ACS OMEGA

http://pubs.acs.org/journal/acsodf

Article

Ulothrix-Derived Sulfur-Doped Porous Carbon for High-Performance Symmetric Supercapacitors

Song Liu, Kun Chen, Qiang Wu, Yuanyuan Gao, Changguo Xue,* and Xiang Dong

Cite This: *ACS Omega* 2022, 7, 10137−10143

Read Online

ACCESS | Metrics & More | Article Recommendations | Supporting Information

ABSTRACT: With the demand for carbon dioxide emission reduction, the sustainable conversion of useless biomass into high-value energy storage devices has received excellent scientific and technological attention. The high synthesis cost and low specific capacitance limited the supercapacitor application. Therefore, biomass-derived sulfur-doping porous carbon (SPC) has been synthesized from ulothrix using simple pyrolysis and chemical activation methods. The unique activated carbon material exhibits a high specific surface area (2490 m^2 g^{-1}), and the effect of the activator addition ratio was systematically investigated. The optimized SPC-2 displayed a high specific capacitance (324 F g^{-1} at 1 A g^{-1}) and excellent cycling stability (90.6% retention after 50 000 cycles). Furthermore, a symmetric supercapacitor (SSC) based on SPC-2 demonstrated a high energy density (12.9 Wh kg^{-1}) at an 800 W kg^{-1} power density. This work offers a simple, economical, and ecofriendly synthetic strategy of converting widespread, useless biomass waste into high-performance supercapacitor applications.

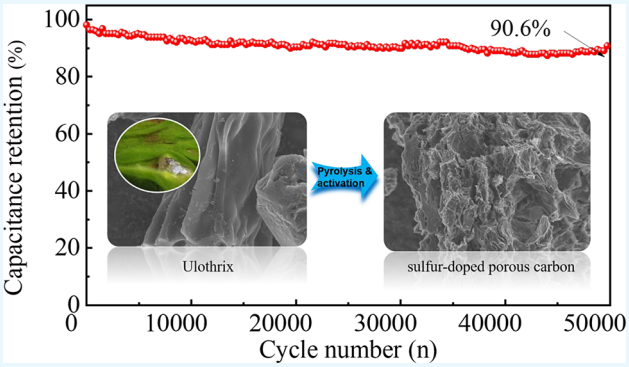

1. INTRODUCTION

With the increasing demand for portable power storage systems in automobiles, electronic goods, and capital machinery, researchers have expended a great amount of effort to develop electric energy storage devices with high energy density and output power. As a novelty electric device filling the gap between batteries and traditional capacitors, supercapacitors have satisfactory energy densities and power densities.[1] The performance of supercapacitors depends mainly on the electrode materials, and a variety of novel nanostructured carbon materials have been widely adopted.[2] They can be classified into electrical double-layer capacitors (EDLCs)[3] according to the charge-storage mechanism, and another type consists of pseudocapacitors. For these electrical double-layer carbon materials, a large surface, suitable pore structure, and high conductivity are essential to storing electric charge.

To meet these requirements, researchers mainly consider the improvement from the aspects of proper carbon sources,[4] the activation procedure,[5] and heteroatom doping.[6] Many kinds of precursors were selected as carbon sources to boost the surface properties, such as biomass-derived carbon,[7−10] polymer-derived carbon,[11,12] carbide-derived carbon,[13] and MOF-templated carbon.[14,15] Among these, biomass has been taken into account by many researchers because of its large specific area, abundant pore structure, ecofriendliness, and extensive sources.[16] For example, various biomass products such as walnut shells,[17,18] pomelo peels,[19] bamboo bagasse,[20] willow catkins,[21] cornstalks,[22] bean curds,[23] and garlic seeds[24] were made into porous carbon. Woody biomass mainly consists of cellulose, hemicellulose, and lignin.[25]

Activation is a crucial process for pore formation in biomass materials.[26] A large amount of carbon exists in the heating process and maintains its original morphology, which is the best natural template.[27,28] Meanwhile, gases escape, forming channels. After chemical activation, biomass becomes porous carbon with large specific surface areas and develops a pore structure.

Besides, biomass carbon has the advantage of self-doping because these natural products have many organic substances. The tissues can convert to heteroatom doping in the carbon matrix during pyrolysis, avoiding extra reagents. And these heteroatoms, such as nitrogen,[29] oxygen, sulfur,[30] and phosphorus,[31] can efficiently enhance electrical conductivity and wettability.

Ulothrix is widely grown in most parts of our planet, and its excessive growth is often regarded as a sign of water body eutrophication. The government pays the bill to clean it up

Received: November 7, 2021
Accepted: March 8, 2022
Published: March 17, 2022

https://doi.org/10.1021/acsomega.1c06253
ACS Omega 2022, 7, 10137−10143

Scheme 1. Illustration of the Synthesis Process of SPC

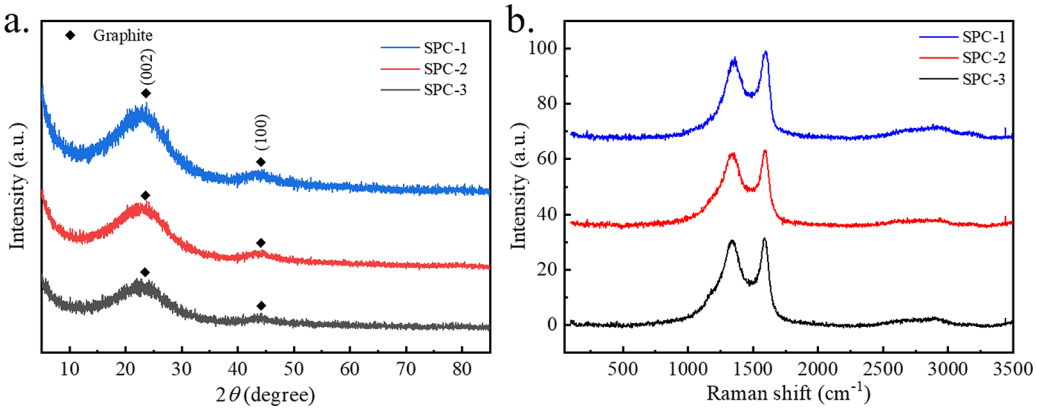

Figure 1. (a) XRD patterns and (b) Raman spectra of the SPC.

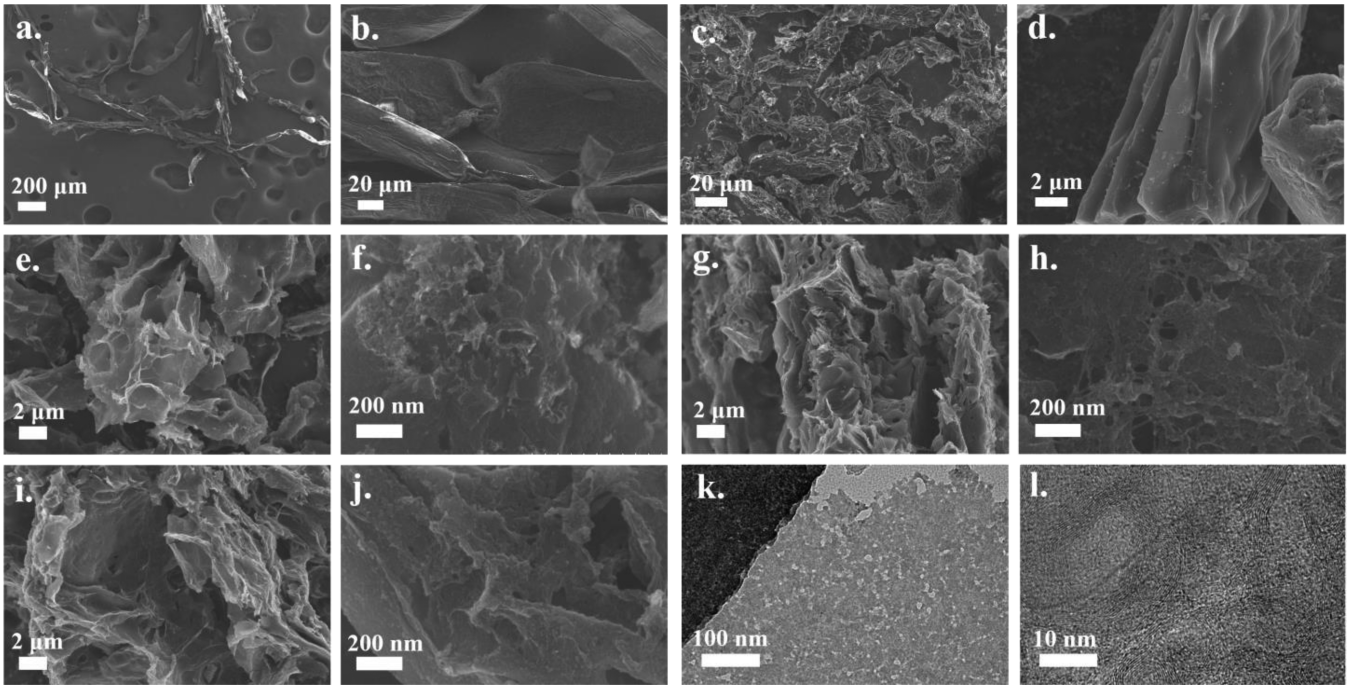

Figure 2. SEM images of (a, b) ulothrix, (c, d) pyrolytic carbon, (e, f) SPC-1, (g, h) SPC-2, and (i, j) SPC-3. (k, l) TEM images of SPC-2.

every year, whereas it has potential resource utilization value. As shown in Scheme 1, ulothrix is green and filiform, serving as the natural template for carbon microbelts. The floristic stoma, along with the abundant pores formed in the carbonization and activation process, results in rich hierarchical apertures. In addition, fibrin and amino acids in the plant tissue can be considered to be sulfur and nitrogen species to obtain self-doping carbon materials. These doped atoms can efficiently enhance the conductivity of carbon skeletons, which is helpful for electrochemical performance.

Herein, a sulfur-doped porous carbon with a large specific surface area is obtained by pyrolysis and following chemical

https://doi.org/10.1021/acsomega.1c06253
ACS Omega 2022, 7, 10137−10143

activation. The unique characterizations of the SPC are the following: (i) ulothrix with a proper microbelt shape and rich organic matter is selected as the natural template; (ii) the synthetic process is simple and easy without the use of extra temples and a postdoping procedure; and (iii) the carbon product has a large surface area and uniform sulfur doping. Such a low-cost, ecofriendly, high-performance carbon converted from useless plant tissue to a high-value product is economically beneficial and highly feasible.

2. RESULTS AND DISCUSSION

2.1. Characterization of Materials. An illustration of the synthesis of the SPC is shown in Scheme. 1. By cleanly heating ulothrix in an inert atmosphere at 500 °C for 1 h, the pyrolytic carbon powder was prepared. Then the pyrolytic carbon mixed with KOH was heated to 800 °C for 2 h. Finally, the SPC was acquired by using excess hydrochloric acid, washing the products until the pH was below 7, and drying in vacuum at 80 °C for 12 h. The XRD patterns of the SPC samples are shown in Figure 1a, and all three curves show two typical diffraction peaks at 24 and 43°, corresponding to the (002) and (100) planes of the graphite phase (PDF no. 89-8487). These weak, broad peaks indicate that after pyrolysis and activation the SPC is considered to be amorphous carbon with a low degree of graphitization.[32] The Raman spectra (shown in Figure 1b) of SPC samples exhibit two base peaks at 1340 and 1595 cm^{-1}, which correspond to the disordered graphite carbon phase (D band) and the graphitic carbon phase (G band),[33] respectively. The intensity ratios of the D/G band for SPC-1, SPC-2, and SPC-3 are 0.929, 0.963, and 0.974, indicating the imperfect structure of the graphitic carbon.[34]

The morphology of the samples was explored by using the SEM (Figure 2). It is clear that the clean ulothrix (Figure 2a,b) displays a belt shape that is about 40−80 μm wide and a few micrometers thick. After pyrolysis (Figure 2c,d), the particles displayed many wrinkles on a smooth surface as the plant tissues lost water. By comparison, SEM images of the activated SPC samples are shown in Figure 2e−j. All SPC samples indicate many small irregular particles with hierarchical pore structure, and various sizes of holes and channels can be found. It is clear that mesopores of a few nanometer sizes can be found in the high-resolution image of SPC-1 (Figure 2f), resulting from the high-temperature activation process. For SPC-2 and SPC-3, there were more pores on the surface. TEM images further display the mesoporous structure of the carbon sheets (Figure 2k,l). The specific surface areas, pore size distributions, and pore volumes of the SPC samples are calculated on the basis of the N_2 adsorption test results (Table 1). The specific surface areas of SPC-1−SPC-3 are 1944, 2490, and 2018 $m^2\ g^{-1}$, and the pore size distributions of SPC-1−SPC-3 are located at 4.32, 5.33, and 6.10 nm, respectively, revealing the mesoporous structure in the carbon sheets.

Table 1. Specific Surface Areas, Pore Size Distributions, and Pore Volumes of SPC

sample	surface area ($m^2\ g^{-1}$)	pore volume ($cc\ g^{-1}$)	pore diameter (nm)
SPC-1	1944	0.615	4.32
SPC-2	2018	0.532	5.33
SPC-3	2490	0.835	6.10

Nitrogen adsorption/desorption isotherms and pore size distribution diagrams are shown in Figure S1.

To verify the elemental makeup of the samples, XPS measurements were conducted, and the spectra of SPC-2 are shown in Figure 3. The C, O, and S element contents (atom %) are 79.74, 16.46, and 2.2%, respectively. The full spectrum shows obvious O 1s, C 1s, and S 2p peaks. The C 1s narrow peak can be indexed to the fitting peaks at 288.64, 285.96, and 284.67 eV, and the S 1s peak can be fitted to three peaks: S1 at 163.8, S2 at 164.9, and S3 at 168.7 eV. The S1 and S2 peaks correspond to S $2p_{3/2}$ and S $2p_{1/2}$ of the C−S_x−C covalent bond, and the S3 peak can be indexed to the oxidized sulfur C−SO_x−C bond following previous reports.[30,35,36] For the O 1s spectrum, the O1 peak at 531.87 eV can be attributed to the carbon−oxygen bond (C═O). The O2 peak at 533.23 eV corresponds to the binding energies of oxygenated C−S functionalities (C−S−O).[25] These results demonstrate that sulfur atoms are successfully incorporated into the carbon network and play an essential role in enhancing the electrochemical performance of SPC.

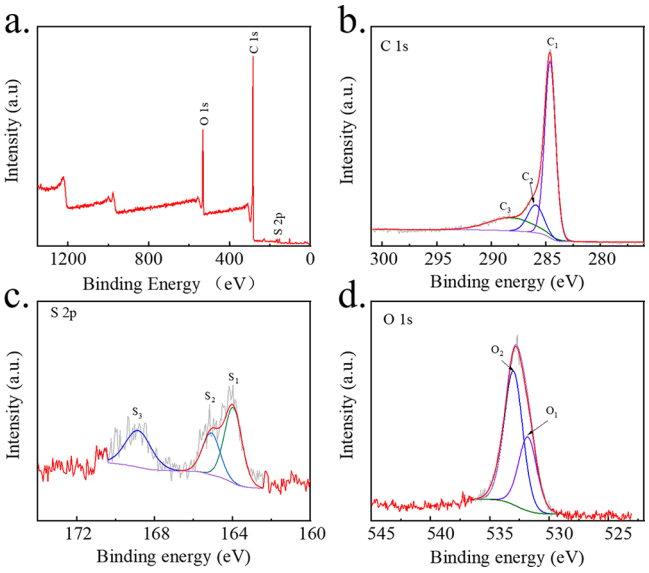

Figure 3. (a) XPS survey spectrum and high-resolution scans of (b) C 1s, (c) S 1s, and (d) O 1s of SPC-2.

2.2. Electrochemical Performance of the SPC Electrodes. The electrochemical performance of SPC electrodes was first evaluated by CV measurement. As shown in Figure 4a, all of the CV curves at a scan rate of 100 mV s^{-1} have a rectangular shape, indicating typical electric double-layer capacitor behavior. The CV curves at different scan rates of SPC-1 and SPC-3 are shown in Figure S2. Among them, SPC-2 has the highest oxidation peak and the largest enclosed area. The GCD measurement resulting in a current density of 1 A g^{-1} are performed in Figure 4b, and all of the GCD curves show a symmetric triangle shape. From the discharge time, the specific capacitance can be acquired. At 1 A g^{-1}, the SPC-1−SPC-3 electrodes have specific capacitances of 97.02, 325.51, and 215.75 F g^{-1}, respectively. The GCD curves at different current densities of SPC-1 and SPC-3 are shown in Figure S3. On the basis of the GCD measurement result, the corresponding specific capacitances of the SPC electrodes at different current densities are shown in Figure 4c. At 0.5 A g^{-1}, the SPC-1−SPC-3 electrodes display the highest specific

https://doi.org/10.1021/acsomega.1c06253
ACS Omega 2022, 7, 10137−10143

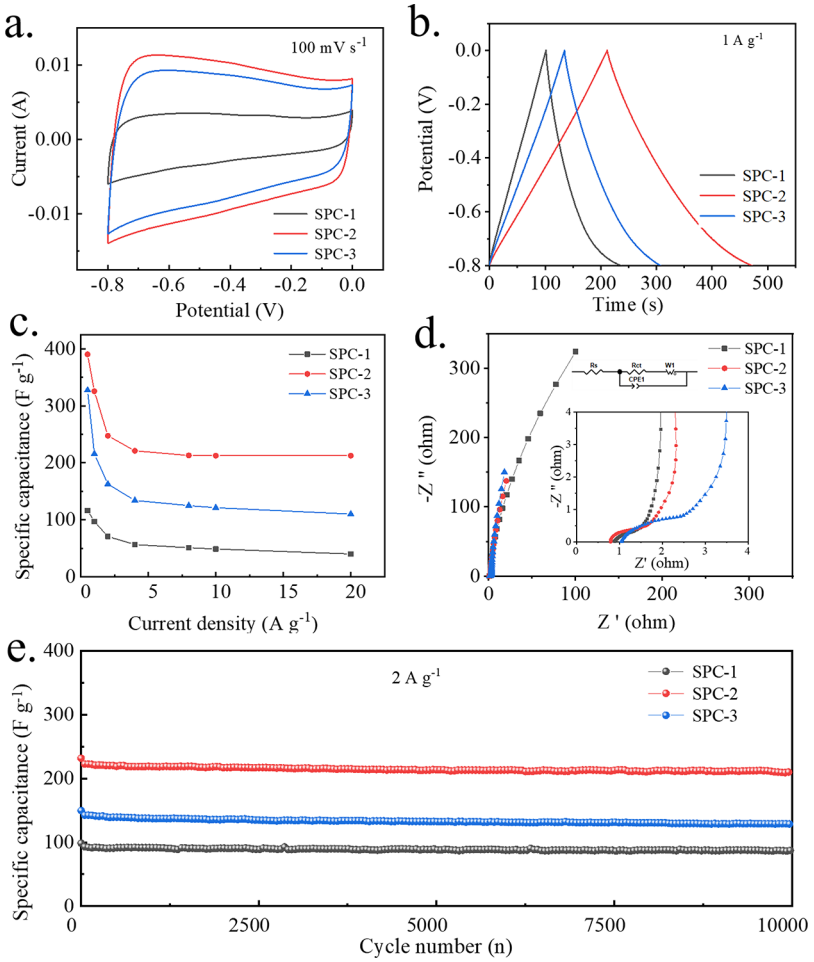

Figure 4. Electrochemical properties of SPC electrodes: (a) CV curves, (b) GCD curves, (c) specific capacitance at different current densities, (d) Nyquist plots (the inset shows a close-up part of the high-frequency region and the stimulated diagram of the equivalent circuit), and (e) cycling performance.

capacitances of 116.31, 390.38, and 327.50 F g^{-1}. Even at 20 A g^{-1}, the specific capacitances were 40.71, 212.46, and 110.29 F g^{-1}. EIS measurements were performed to estimate the impedance of the SPC electrode (Figure 4d). All of the EIS curves consisted of a steep slope in the low-frequency zone and a depressed semicircle in the high-frequency zone. The charge-transfer resistance (R_{ct}) was fitted by Zview software based on the equivalent circuit inserted in Figure 4d.[37] The charge-transfer resistance (R_{ct}) values of the SPC electrode were 0.21, 0.22, and 0.84 Ω. The intrinsic resistance (R_s) values of the SPC electrode were 0.91, 0.81, and 1.05 Ω. It is clear that SPC-2 has the lowest inherent resistance.

Cycling performance tests were conducted to evaluate the lifespan of the SPC electrodes. As shown in Figure 4e, in 10 000 charge/discharge cycles, the SPC electrodes showed very little decay in electrochemical capacity. After the long cycles, the SPC-1−SPC-3 electrode still retain 88.2, 210.2, and 129.6 F g^{-1}, and the corresponding capacity retentions are 92.0, 91.0, and 87.8%.

Because the SPC-2 electrode exhibited the highest capacity of the studied electrode, it was further estimated at different scan rates (Figure 5a). The oxidation and reduction peak current increased with increasing scan rate. Meanwhile, the curves retain a rectangular shape, suggesting electric double-layer behavior. GCD tests were also performed at different current densities to evaluate the rate performance of SPC-2. As

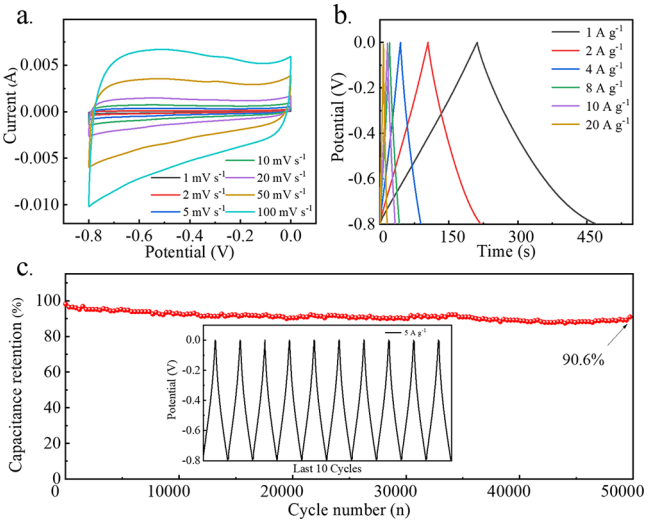

Figure 5. Electrochemical performance of the SPC-2 electrode: (a) CV curves at different scan rates, (b) GCD curves at different current densities, and (c) 50 000 cycling curve at 5 A g^{-1}.

shown in Figure 5b, at current densities of 1, 2, 4, 8, 10, and 20 A g^{-1}, it delivers 325.51, 247.57, 221.04, 213.89, 212.50, and 212.46 F g^{-1}, respectively. The SPC-2 electrode has 73.9%

https://doi.org/10.1021/acsomega.1c06253
ACS Omega 2022, 7, 10137−10143

retention from 2 to 20 A g^{-1}, exhibiting a satisfying rate performance. A cycling test was performed to estimate the lifetime of the SPC-2 electrode, as shown in Figure 5c. A specific capacitance of 211.5 F g^{-1} was obtained after 50 000 long cycles, exhibiting an excellent electrochemical stability of 90.6%.

2.3. Electrochemical Performance of the SSC Device. A symmetric supercapacitor device was fabricated by using SPC-2 as both positive and negative electrodes. The mass ratio of the two electrodes is 1:1. CV scans were performed for the SSC device at 0−1.1 V to 0−1.8 V at 200 mV s^{-1} to determine the upper limit of the voltage range. As shown in Figure 6a,

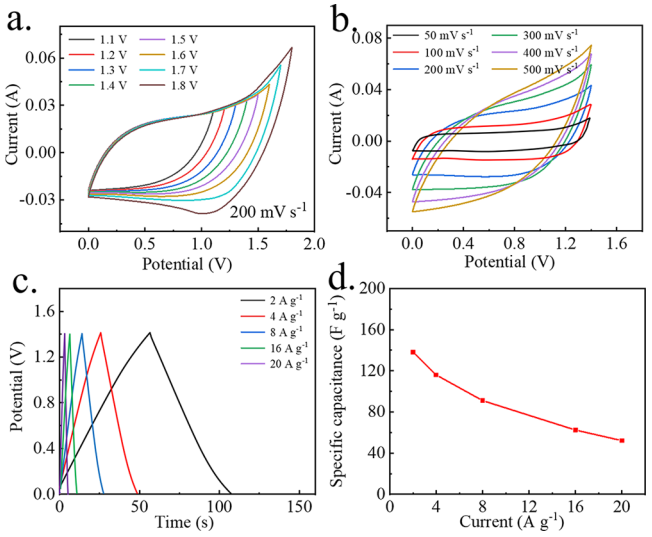

Figure 6. Electrochemical performance of the symmetrical supercapacitor (a) CV curves at different operating potentials, (b) CV curves at different scan rates, (c) GCD curves at different current densities, and (d) specific capacitance at different current densities.

when the voltage surpasses 1.4 V, the current oxidation increases sharply, implying oxygen evolution. For the 1.8 V curve, a weak reduction current peak appeared, indicating a parasitic reaction between the electrolyte and electrode material.[38] As the energy density increases with the working voltage, an operating voltage window of 0−1.4 V was chosen. CV curves at different scan rates are shown in Figure 6b. It can be seen that all of the curves display good capacitive behavior within this range. The GCD curves at different current densities are shown in Figure 6c, and the corresponding specific capacities are plotted in Figure 6d. The SSC device delivered particular capacitances of 138, 116, 91, 63, and 52 F g^{-1} at current densities of 2, 4, 8, 16, and 20 A g^{-1}. In addition, the EIS curves of the ASC are also given (Figure S4). The charge-transfer resistance and intrinsic resistance of the ASC are 2.48 and 2.53 Ω, respectively.

The SSC's energy and power densities are shown in the Ragone plot (Figure 7). The SSC device delivers the highest energy density of 12.9 Wh kg^{-1} at a power density of 800 W kg^{-1} while retaining an energy density of 4.6 Wh kg^{-1} at a power density of 8000 W kg^{-1}. These values are compared to the revealed biomass-derived carbon-based aqueous SSCs properties,[39−45] implying the promising prospect of the SSCs.

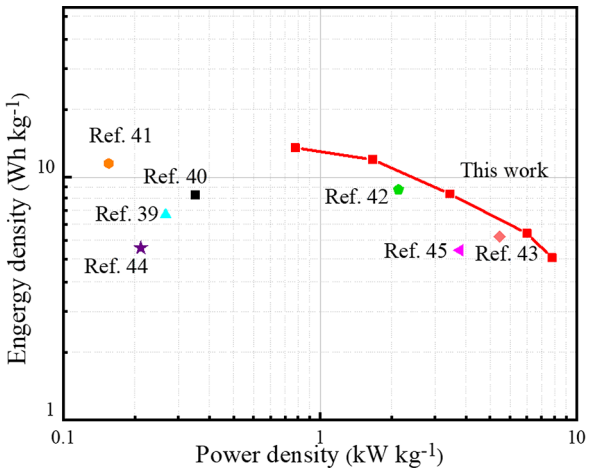

Figure 7. Ragone plot (energy density vs power density) of the symmetrical supercapacitor.

3. CONCLUSION

We have employed facile pyrolysis and then an activation process to synthesize sulfur-doped porous carbon. The SPC materials with a high specific surface area (up to 2490 m^2 g^{-1}) have a high sulfur doping content. The optimized SPC-2 material displays the largest specific capacity (324 F g^{-1} at 1 A g^{-1}) and excellent long cycling performance (90.6% retention after 50 000 cycles). Furthermore, a symmetric supercapacitor based on SPC-2 demonstrated the highest energy density (12.9 Wh kg^{-1}) and the highest power density of 8000 W kg^{-1}, showing promising application prospects.

4. EXPERIMENTAL SECTION

4.1. Synthesis of the Mesoporous Carbon. Ulothrix was collected from the Anhui University of Science and Technology campus. First, the clean, dry ulothrix was pyrolyzed in an N_2 atmosphere at 500 °C for 1 h. After that, the samples were mixed and ground with KOH powder in a mortar with mass ratios of 1:1, 1:2, and 1:3. Then the mixtures were activated in the N_2 atmosphere at 800 °C for 1 h at a 3 °C min^{-1} heating rate. After cooling to room temperature, the samples were washed several times with excess 2 M HCl solution and deionized water. Finally, the products were dried overnight in a vacuum at 120 °C. The as-prepared activated porous carbons were named SPC-1, SPC-2, and SPC-3.

4.2. Characterization of Materials. The SPC samples were characterized by using a powder X-ray diffractometer (Smartlab SE, Cu Kα radiation), SEM (Hitachi, Flex-SEM1000), and Raman spectroscopy (Renishaw, inVia). The specific surface areas of the samples were characterized by using a surface area and porosimetry analyzer (Gold APP Instruments Co. Ltd., V-Sorb 2800P). The SPC samples were also studied by using an X-ray photoelectron spectrometer (ThermoFisher Scientific, ESCALAB 250Xi).

4.3. Electrochemical Measurements. The working electrode was prepared by milling the SPC sample with poly(vinylidene fluoride) (binder, 10 wt %) in *N*-methyl-2-pyrrolidinone to form a homogeneous slurry. Then, the slurry was spread on a piece of Ni foam (1 × 1 cm^2) and dried under vacuum at 80 °C overnight. After that, a Hg/HgO electrode and a Pt foil were used as the hreference electrode and counter electrode in a 2 M KOH electrolyte.

https://doi.org/10.1021/acsomega.1c06253
ACS Omega 2022, 7, 10137−10143

Cyclic voltammetry (CV), chronopotentiometry (CP), and electrochemical impedance spectroscopy (EIS) tests were conducted on a CHI660E electrochemical workstation to evaluate the electrochemical performance of the electrde. The cycling stability performance tests were conducted on a CT2001A LAND battery test system. The qualities of active materials were acquired from the mass change of the Ni foam, and the average loading mass was about 2 mg cm^{-2}.

A symmetric supercapacitor was fabricated by using the SPC as both positive and negative electrodes. A piece of cellulose paper was used as a separator, and a 2 M KOH solution was used as the electrolyte. The specific capacitance of the symmetric supercapacitor was calculated on the basis of the total mass of the active materials, and the calculation formulas of the specific capacitance, energy density, and power density are shown in the Supporting Information.

■ ASSOCIATED CONTENT

Supporting Information

The Supporting Information is available free of charge at https://pubs.acs.org/doi/10.1021/acsomega.1c06253.

Equations of specific capacitance, energy density, and power density; N_2 adsorption/desorption isotherms and pore size distributions of SPC; CV curves of SPC-1 and SPC-3; GCD curves of SPC-1 and SPC-3; and EIS curve of SSC (PDF)

■ AUTHOR INFORMATION

Corresponding Author

Changguo Xue − *School of Materials Science and Engineering, Anhui University of Science and Technology, Huainan, Anhui, China 232001;* orcid.org/0000-0001-9671-5542; Email: chgxue@aust.edu.cn

Authors

Song Liu − *School of Materials Science and Engineering, Anhui University of Science and Technology, Huainan, Anhui, China 232001*

Kun Chen − *School of Materials Science and Engineering, Anhui University of Science and Technology, Huainan, Anhui, China 232001*

Qiang Wu − *School of Materials Science and Engineering, Anhui University of Science and Technology, Huainan, Anhui, China 232001*

Yuanyuan Gao − *School of Materials Science and Engineering, Anhui University of Science and Technology, Huainan, Anhui, China 232001*

Xiang Dong − *School of Safety Science and Engineering, Anhui University of Science and Technology, Huainan, Anhui, China 232001;* orcid.org/0000-0002-6981-1691

Complete contact information is available at: https://pubs.acs.org/10.1021/acsomega.1c06253

Notes

The authors declare no competing financial interest.

■ ACKNOWLEDGMENTS

This work was supported by the National Natural Science Foundation of China (grant nos. 11872001 and 12172002), the Excellent Youth Foundation of Anhui Scientific Committee (grant no. 1808085J30), the Key Research and Development Program Projects in Anhui Province 2020 (grant no. 202004h07020026), the University-Level Key Projects of Anhui University of Science and Technology (QN2018103), the Innovation Foundation for Postgraduate of Anhui University of Science and Technology (2021CX2090), and the National College Students Innovation and Entrepreneurship Training Program (S202010361168).

■ REFERENCES

(1) Simon, P.; Gogotsi, Y. Materials for electrochemical capacitors. *Nat. Mater.* **2008**, *7*, 845−854.

(2) Gu, W.; Yushin, G. Review of nanostructured carbon materials for electrochemical capacitor applications: advantages and limitations of activated carbon, carbide-derived carbon, zeolite-templated carbon, carbon aerogels, carbon nanotubes, onion-like carbon, and graphene. *WIREs Energy Environ.* **2014**, *3*, 424−473.

(3) Simon, P.; Gogotsi, Y.; Dunn, B. Where Do Batteries End and Supercapacitors Begin? *Science* **2014**, *343*, 1210−1211.

(4) Gandla, D.; Wu, X.; Zhang, F.; Wu, C.; Tan, D. Q. High-Performance and High-Voltage Supercapacitors Based on N-Doped Mesoporous Activated Carbon Derived from Dragon Fruit Peels. *ACS Omega* **2021**, *6*, 7615−7625.

(5) Song, M.; Zhou, Y.; Ren, X.; Wan, J.; Du, Y.; Wu, G.; Ma, F. Biowaste-based porous carbon for supercapacitor: The influence of preparation processes on structure and performance. *J. Colloid Interface Sci.* **2019**, *535*, 276−286.

(6) Liu, M. Y.; Niu, J.; Zhang, Z. P.; Dou, M. L.; Wang, F. Potassium compound-assistant synthesis of multi-heteroatom doped ultrathin porous carbon nanosheets for high performance supercapacitors. *Nano Energy* **2018**, *51*, 366−372.

(7) Yang, L.; Wang, J.; Wang, S.; Guan, X.; Guan, X.; Wang, G. Biomass-derived multi-heteroatom-doped carbon materials for high-performance solid-state symmetric supercapacitors with superior long-term cycling stability. *Ionics* **2020**, *26*, 4141−4151.

(8) Zhu, Y.; Chen, M.; Zhang, Y.; Zhao, W.; Wang, C. A biomass-derived nitrogen-doped porous carbon for high-energy supercapacitor. *Carbon* **2018**, *140*, 404−412.

(9) Moustafa, E.; El Nady, J.; Kashyout, A. E. H. B.; Shoueir, K.; El-Kemary, M. Fabrication of High Yield Photoluminescent Quantized Graphene Nanodiscs for Supercapacitor Devices. *ACS Omega* **2021**, *6*, 23090−23099.

(10) Raut, S. D.; Shinde, N. M.; Nakate, Y. T.; Ghule, B. G.; Gore, S. K.; Shaikh, S. F.; Pak, J. J.; Al-Enizi, A. M.; Mane, R. S. Coconut-Water-Mediated Carbonaceous Electrode: A Promising Eco-Friendly Material for Bifunctional Water Splitting Application. *ACS Omega* **2021**, *6*, 12623−12630.

(11) Xin, S.; Yang, N.; Gao, F.; Zhao, J.; Li, L.; Teng, C. Three-dimensional polypyrrole-derived carbon nanotube framework for dye adsorption and electrochemical supercapacitor. *Appl. Surf. Sci.* **2017**, *414*, 218−223.

(12) Bello, A.; Barzegar, F.; Madito, M. J.; Momodu, D. Y.; Khaleed, A. A.; Masikhwa, T. M.; Dangbegnon, J. K.; Manyala, N. Electrochemical performance of polypyrrole derived porous activated carbon-based symmetric supercapacitors in various electrolytes. *Rsc Adv.* **2016**, *6*, 68141−68149.

(13) Largeot, C.; Portet, C.; Chmiola, J.; Taberna, P. L.; Gogotsi, Y.; Simon, P. Relation between the ion size and pore size for an electric double-layer capacitor. *J. Am. Chem. Soc.* **2008**, *130*, 2730−2731.

(14) Xu, D.; Ding, Q.; Li, J.; Chen, H.; Pan, Y.; Liu, J. A sheet-like MOF-derived phosphorus-doped porous carbons for supercapacitor electrode materials. *Inorg. Chem. Commun.* **2020**, *119*, 108141.

(15) Xu, X.; Yang, T.; Zhang, Q.; Xia, W.; Ding, Z.; Eid, K.; Abdullah, A. M.; Hossain, M. S. A.; Zhang, S.; Tang, J.; Pan, L.; Yamauchi, Y. Ultrahigh capacitive deionization performance by 3D interconnected MOF-derived nitrogen-doped carbon tubes. *Chem. Eng. J.* **2020**, *390*, 124493.

(16) Li, Z.; Guo, D.; Liu, Y.; Wang, H.; Wang, L. Recent advances and challenges in biomass-derived porous carbon nanomaterials for supercapacitors. *Chem. Eng. J.* **2020**, *397*, 125418.

(17) Xu, X.; Gao, J.; Tian, Q.; Zhai, X.; Liu, Y. Walnut shell derived porous carbon for a symmetric all-solid-state supercapacitor. *Appl. Surf. Sci.* **2017**, *411*, 170−176.
(18) Qiu, X.; Wang, L.; Zhu, H.; Guan, Y.; Zhang, Q. Lightweight and efficient microwave absorbing materials based on walnut shell-derived nano-porous carbon. *Nanoscale* **2017**, *9*, 7408−7418.
(19) Fu, G. S.; Li, Q.; Ye, J. L.; Han, J. J.; Wang, J. Q.; Zhai, L.; Zhu, Y. W. Hierarchical porous carbon with high nitrogen content derived from plant waste (pomelo peel) for supercapacitor. *J. Mater. Sci. Mater. Electron.* **2018**, *29*, 7707−7717.
(20) Tian, W.; Gao, Q.; Tan, Y.; Yang, K.; Zhu, L.; Yang, C.; Zhang, H. Bio-inspired beehive-like hierarchical nanoporous carbon derived from bamboo-based industrial by-product as a high performance supercapacitor electrode material. *J. Mater. Chem. A* **2015**, *3*, 5656−5664.
(21) Xie, L. J.; Sun, G. H.; Su, F. Y.; Guo, X. Q.; Kong, Q. Q.; Li, X. M.; Huang, X. H.; Wan, L.; Song, W.; Li, K. X.; Lv, C. X.; Chen, C. M. Hierarchical porous carbon microtubes derived from willow catkins for supercapacitor applications. *J. Mater. Chem. A* **2016**, *4*, 1637−1646.
(22) Li, J.; Jiang, Q.; Wei, L.; Zhong, L.; Wang, X. Simple and scalable synthesis of hierarchical porous carbon derived from cornstalk without pith for high capacitance and energy density. *J. Mater. Chem. A* **2020**, *8*, 1469−1479.
(23) Li, Q.; Wu, X. Z.; Zhao, Y.; Miao, Z. C.; Xing, L. B.; Zhou, J.; Zhao, J. P.; Zhuo, S. P. Nitrogen-Doped Hierarchical Porous Carbon through One-Step Activation of Bean Curd for High-Performance Supercapacitor Electrode. *Chemelectrochem* **2018**, *5*, 1606−1614.
(24) Li, S.; Chen, Q.; Gong, Y.; Wang, H.; Li, D.; Zhang, Y.; Fu, Q.; Pan, C. One-Step" Carbonization Activation of Garlic Seeds for Honeycomb-like Hierarchical Porous Carbon and Its High Supercapacitor Properties. *ACS Omega* **2020**, *5*, 29913−29921.
(25) Deng, Q.; Abbas, S. C.; Li, Z.; Lv, J.; Ma, X.; Cao, S.; Ni, Y.; Zhao, W. Chemically modified self-doped biocarbon via novel sulfonation assisted sacrificial template method for high performance flexible all solid-state supercapacitor. *J. Colloid Interface Sci.* **2020**, *574*, 33−42.
(26) Lu, H.; Zhao, X. S. Biomass-derived carbon electrode materials for supercapacitors. *Sustain. Energy Fuels* **2017**, *1*, 1265−1281.
(27) Zhang, L. X.; Liu, Z. H.; Cui, G. L.; Chen, L. Q. Biomass-derived materials for electrochemical energy storages. *Prog. Polym. Sci.* **2015**, *43*, 136−164.
(28) Wang, Y. L.; Qu, Q. L.; Gao, S. T.; Tang, G. S.; Liu, K. M.; He, S. J.; Huang, C. B. Biomass derived carbon as binder-free electrode materials for supercapacitors. *Carbon* **2019**, *155*, 706−726.
(29) Lin, T.; Chen, I. W.; Liu, F.; Yang, C.; Bi, H.; Xu, F.; Huang, F. Nitrogen-doped mesoporous carbon of extraordinary capacitance for electrochemical energy storage. *Science* **2015**, *350*, 1508−1513.
(30) Li, Y. J.; Wang, G. L.; Wei, T.; Fan, Z. J.; Yan, P. Nitrogen and sulfur co-doped porous carbon nanosheets derived from willow catkin for supercapacitors. *Nano Energy* **2016**, *19*, 165−175.
(31) Fragal, V. H.; Fragal, E. H.; da Silva, E. P.; Acerce, M.; Chhowalla, M.; Rubira, A. F.; Tambourgi, E. B.; Asefa, T.; Silva, R. Nitrogen and Phosphorus Co-doped Nanoporous Carbons from Phosphoprotein/Silica Self-Assemblies for Energy Storage in Supercapacitors. *Chemelectrochem* **2020**, *7*, 4773−4781.
(32) Ma, F. W.; Wan, J. F.; Wu, G.; Zhao, H. Highly porous carbon microflakes derived from catkins for high-performance supercapacitors. *Rsc Adv.* **2015**, *5*, 44416−44422.
(33) Su, X. L.; Chen, J. R.; Zheng, G. P.; Yang, J. H.; Guan, X. X.; Liu, P.; Zheng, X. C. Three-dimensional porous activated carbon derived from loofah sponge biomass for supercapacitor applications. *Appl. Surf. Sci.* **2018**, *436*, 327−336.
(34) Mazurenko, I.; Etienne, M.; Francius, G.; Vakulko, I.; Walcarius, A. Macroporous carbon nanotube-carbon composite electrodes. *Carbon* **2016**, *109*, 106−116.
(35) Zhou, C. L.; Wang, D. K.; Li, A.; Pan, E. Z.; Liu, H. Y.; Chen, X. H.; Jia, M. Q.; Song, H. H. Three-dimensional porous carbon doped with N, O and P heteroatoms as high-performance anode materials for sodium ion batteries. *Chem. Eng. J.* **2020**, *380*, 122457.
(36) Hao, E.; Liu, W.; Liu, S.; Zhang, Y.; Wang, H.; Chen, S.; Cheng, F.; Zhao, S.; Yang, H. Rich sulfur doped porous carbon materials derived from ginkgo leaves for multiple electrochemical energy storage devices. *J. Mater. Chem. A* **2017**, *5*, 2204−2214.
(37) Liu, K.; Zhang, J.; Ding, R.; Zheng, X.; Yang, T.; Wang, C.; Chen, M. Potassium-assisted carbonization of pyrrole to prepare nanorod-structured graphitic carbon with a high surface area for high-rate supercapacitors. *Carbon* **2019**, *155*, 326−333.
(38) Mathis, T. S.; Kurra, N.; Wang, X. H.; Pinto, D.; Simon, P.; Gogotsi, Y. Energy Storage Data Reporting in Perspective—Guidelines for Interpreting the Performance of Electrochemical Energy Storage Systems. *Adv. Energy Mater.* **2019**, *9*, 1902007.
(39) Tripathy, A.; Mohanty, S.; Nayak, S. K.; Ramadoss, A. Renewable banana-peel-derived activated carbon as an inexpensive and efficient electrode material showing fascinating supercapacitive performance. *J. Environ. Chem. Eng.* **2021**, *9*, 106398.
(40) Raj, C. J.; Manikandan, R.; Rajesh, M.; Sivakumar, P.; Jung, H.; Das, S. J.; Kim, B. C. Cornhusk mesoporous activated carbon electrodes and seawater electrolyte: The sustainable sources for assembling retainable supercapacitor module. *J. Power Sources* **2021**, *490*, 229518.
(41) Qu, K.; Wang, W.; Shi, C.; Sun, Z.; Qi, H.; Shi, J.; Yang, S.; Huang, Z.; Guo, Z. Fungus bran-derived nanoporous carbon with layered structure and rime-like support for enhanced symmetric supercapacitors. *J. Nanostructure Chem.* **2021**, *11*, 769−784.
(42) Mehare, M. D.; Deshmukh, A. D.; Dhoble, S. J. Preparation of porous agro-waste-derived carbon from onion peel for supercapacitor application. *J. Mater. Sci.* **2020**, *55*, 4213−4224.
(43) Huang, Y.; Peng, L.; Liu, Y.; Zhao, G.; Chen, J. Y.; Yu, G. Biobased Nano Porous Active Carbon Fibers for High-Performance Supercapacitors. *ACS Appl. Mater. Interfaces* **2016**, *8*, 15205−15215.
(44) Teo, E. Y. L.; Muniandy, L.; Ng, E. P.; Adam, F.; Mohamed, A. R.; Jose, R.; Chong, K. F. High surface area activated carbon from rice husk as a high performance supercapacitor electrode. *Electrochim. Acta* **2016**, *192*, 110−119.
(45) Wahid, M.; Puthusseri, D.; Phase, D.; Ogale, S. Enhanced Capacitance Retention in a Supercapacitor Made of Carbon from Sugarcane Bagasse by Hydrothermal Pretreatment. *Energy Fuels* **2014**, *28*, 4233−4240.

https://doi.org/10.1021/acsomega.1c06253
ACS Omega 2022, 7, 10137−10143